Journal of Molecular Structure 1253 (2022) 132289

Contents lists available at ScienceDirect

Journal of Molecular Structure

journal homepage: www.elsevier.com/locate/molstr

Synthesis and antifungal activity of nitrophenyl-pyrazole substituted Schiff bases

Andrés Restrepo-Acevedo[a,b], Nicolas Osorio[a], Luis E. Giraldo-López[a], Richard F. D'Vries[c], Susana Zacchino[d], Rodrigo Abonia[e], Ronan Le Lagadec[b,*], Fernando Cuenú-Cabezas[a,*]

[a] Laboratorio de Química Inorgánica y Catálisis, Programa de Química., Universidad del Quindío, Carrera 15, Calle 12 Norte, Armenia, Colombia
[b] Instituto de Química UNAM, Circuito Exterior s/n, Ciudad Universitaria, 04510 Ciudad de México, Mexico
[c] Facultad de Ciencias Básicas, Universidad Santiago de Cali, Calle 5 # 62-00, Cali, Colombia
[d] Área Farmacognosia, Facultad de Ciencias Bioquímicas y Farmacéuticas, Universidad Nacional de Rosario, Suipacha 531, 2000 Rosario, Argentina
[e] Departamento de Química, Universidad del Valle, Calle 13 No. 100-00, A.A. 25360, Cali, Colombia

ARTICLE INFO

Article history:
Received 28 October 2021
Revised 3 December 2021
Accepted 25 December 2021
Available online 27 December 2021

Keywords:
Ab initio calculations
Antifungal agents
Nitrogen heterocycles
Nitrophenyl
Schiff bases

ABSTRACT

Three new pyrazole-based azomethine isomers (**2a-c**) bearing a 2-, 3- or 4-nitrophenyl substituent were prepared in almost quantitative yields using environmentally friendly techniques such as solvent-free and microwave-assisted procedures. The compounds were fully characterized by standard analytical methods, including single-crystal X-ray diffraction crystallography for two of the three synthesized compounds. The calculated molecular orbitals distributions of the HOMO and LUMO show that the band gap energy can be tuned by the addition of a nitrophenyl group on the pyrazole moiety and therefore the electrophilic character and the reactivity of the Schiff bases. The relative position of the nitro group plays an important role on the antifungal activity against *C. albicans* as compound bearing the 2-nitrophenyl substituent (**2a**) was considerably more active than the other derivatives. In contrast, all three isomers presented a similar, limited, activity against *C. neoformans*. Molecular docking simulations showed that the most active compound **2a** presented the lowest binding energy with 3PVK model protein.

1. Introduction

Pyrazole derivatives of Schiff bases containing a phenol ring in their structure have been applied in a wide variety of biological studies [1–3] and have exhibited valuable physicochemical properties such as photochromism [4–7], thermochromism [8], and solvatochromism [9–11]. On the other hand, pyrazoles and Schiff bases are widely used as ligands in the formation of metal complexes, which in turn have extensively been studied for potential applications in medicine [12–17]. The incidence of fungal infections (mycoses) has showed a steady increase over the past two decades, becoming a major cause of morbidity and mortality [2]. Unfortunately, mycoses are often problematic to diagnose and treat. Despite the availability of antimycotic agents, critically ill and susceptible patients are commonly difficult to treat. The main reasons for this include delayed diagnosis, drug toxicity, development of drug resistance and bioavailability of the drug. Immunocompromised patients, especially transplant recipients, are notably vulnerable as mycoses can grow rapidly and infection spreads quickly, causing complications in treatments [18].

For several years, our research group has been involved in the chemistry of pyrazole-based azomethine derivatives, with a specific interest in studying the influence of the substitution pattern on the potential biological activities of the compounds [19–23]. Of particular significance is the presence of the nitro group which, despite concerns about the toxicity related to compounds containing the nitro-moiety [3], has widely been studied in the development of new therapeutic drugs [24]. In fact, many approved drugs contain nitro groups, especially antibiotics which rely on the ability of this type of compounds to impede the replication of microorganisms [25,26]. The nitro group is a strong electron-withdrawing moiety and as a consequence, sections of the molecules become less polar, resulting in nonpolar interactions with important proteins [24]. Additionally, it is known than nitro groups can undergo reduction under physiological conditions [27]. However, the ease of such redox processes depends on the regiochemistry, and in particular, on the position of the nitro group in aromatic rings, as described for nitrobenzene derivatives [28]. These facts led us to study the influence of nitro-substitution in pyrazole-based azomethines to optimize their potential pharmacological activity.

* Corresponding authors.
E-mail addresses: ronan@unam.mx (R. Le Lagadec), fercuenu@uniquindio.edu.co (F. Cuenú-Cabezas).

https://doi.org/10.1016/j.molstruc.2021.132289
0022-2860/

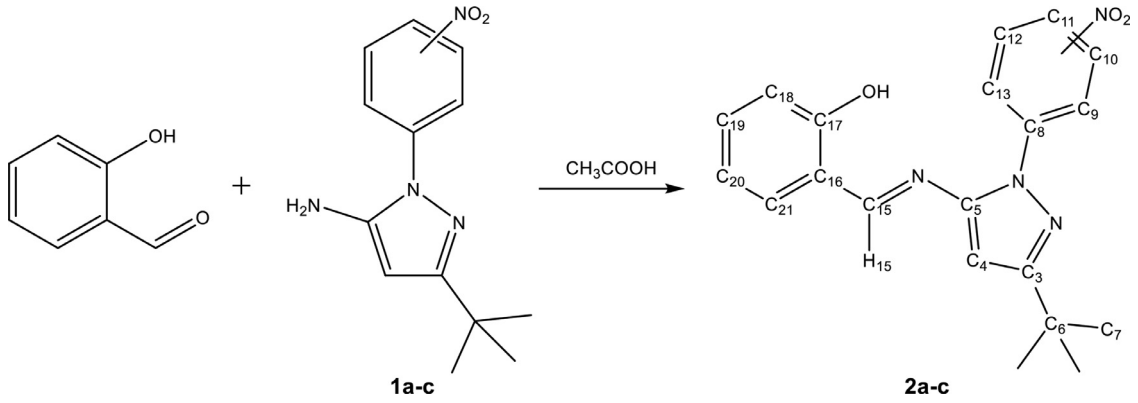

Scheme 1. Synthesis of the 2-hydroxyphenol-based pyrazolic Schiff bases **2a-c** and numbering used for NMR assignment.

In this communication, we present the synthesis of three new azomethine isomers based on a pyrazole moiety bearing a nitrophenyl substituent in different positions and preliminary results on their antifungal activity on *C. albicans* and *C. neoformans*. We also carried out DFT calculations and molecular docking simulations to explore their electronic behavior and draw a possible relationship with their antifungal activity.

2. Experimental

2.1. Materials and reagents

All reagents were purchased from Sigma Aldrich and were used as received. All microwave-assisted reactions were carried out with a CEM focused microwave synthesizer system, model CEM/DISCOVER SP-D working at 100 W. Microanalyses were performed on an Agilent 2400 series II CHNS elemental analyzer. The mass spectra were recorded by the EI technique using a Shimadzu GCMS DI-2010 spectrometer equipped with a direct input probe operating at 70 eV. Infrared spectra were recorded on a Perkin-Elmer FT series 2000 spectrometer using KBr disks. The NMR spectra were recorded on a Bruker Avance spectrometer at 400 MHz for proton and 100 MHz for carbon. All samples contained an internal standard of tetramethylsilane (TMS) in deuterated solvent. NMR spectra splitting patterns were designated as s (singlet), d (doublet), m (multiplet) or br s (broad singlet), as appropriate. All chemical shifts (δ) are quoted as parts per million and the coupling constants (J) are in Hertz (Hz). For NMR assignment the atoms were numbered according to Scheme 1.

2.2. Synthesis

2.2.1. Synthesis of aminopyrazoles

Compounds 3–*tert*–butyl–1-(2-nitrophenyl)–1*H*-pyrazol-5-amine **1a**, 3–*tert*–butyl–1-(3-nitrophenyl)–1*H*-pyrazol-5-amine **1b** and 3–*tert*–butyl–1-(4-nitrophenyl)–1*H*-pyrazol-5-amine **1c** were synthesized following reported methodologies [22,23,29].

2.2.2. Synthesis of Schiff bases

Compounds (*E*)–2-(((3-(*tert*–butyl)–1-(2-nitrophenyl)–1*H*-pyrazol-5-yl)imino)methyl)phenol **2a**, (*E*)–2-(((3-(*tert*–butyl)–1-(3-nitrophenyl)–1*H*-pyrazol-5-yl)imino)methyl)phenol **2b** and (*E*)–2-(((3-(*tert*–butyl)–1-(4-nitrophenyl)–1*H*-pyrazol-5-yl)imino)-methyl)phenol} **2c** were prepared using the following synthetic methodologies: conventional heating, fusion, microwave-assisted synthesis and mechanochemistry. The synthetic procedure for compounds **2a-c** is shown in Scheme 1. In a typical experiment, 200 mg (0.77 mmol) of the respective aminopyrazole **1a-c** and 93.85 mg (0.77 mmol) of 2-hydrozybenzaldehyde were used. All reactions were monitored by TLC and once the reaction was completed, the obtained solid is added to a beaker and stirred at room temperature in 10 mL of a water:ethanol (5:1) solution for 15 min. The solid was filtered off, washed with cold distilled water (4 × 15 mL) and air-dried.

2.2.2.1. Conventional synthesis. the respective aminopyrazole, 2-hydroxybenzaldehyde, 10 drops of acetic acid and 10 mL of ethanol were refluxed for 24 h. After evaporation of the solvent, compounds **2a-c** were purified and isolated as described above. Yield: **2a**, 68%; **2b**, 86%; **2c**, 72%.

2.2.2.2. Fusion. in a test tube, a mixture of the respective aminopyrazole, 2-hydroxybenzaldehyde and 5 drops of acetic acid was slowly heated to 160 °C for 1 h. After cooling to room temperature, compounds **2a-c** were purified and isolated as described above. Yield: **2a**, 95%; **2b**, 98%; **2c**, 98%.

2.2.2.3. Microwave-assisted synthesis. a solution of the respective aminopyrazole, 2-hydroxybenzaldehyde and acetic acid (5 drops) in EtOH (2 mL) was placed in a sealed tube and was irradiated using a CEM microwave synthesizer system at 100 W, three times for 5 min. After cooling in a stream of compressed air, the solution was evaporated in vacuum and purified as described above. Yield: **2a**, 96%; **2b**, 98%; **2c**, 98%.

2.2.2.4. Mechanochemistry. the respective aminopyrazole, 2-hydrozybenzaldehyde and glacial acetic acid (5 drops) were placed in a round-bottom flask and stirred with a spatula for 20 min at room temperature. Compounds **2a-c** were purified and isolated as described above. Yield: **2a**, 84%; **2b,** 94%; **2c**, 94%.

(*E*)–2-(((3-(tert–butyl)–1-(2-nitrophenyl)–1H-pyrazol-5-yl)imino)methyl)phenol ***2a***

Beige solid. M.p. 102–103 °C. Anal. calcd. %C 65.92; %H 5.53; %N 15.38, found: %C 65.86; %H 5.47; %N 15.17 for $C_{20}H_{20}N_4O_3$. MS (70 eV) *m/z* (%) 364 $[M]^+$ (100), 349 $[M-15]^+$ (51.95), 318 $[M-46]^+$ (16.11), 307 $[M-57]^+$ (0.37), 122 (1.66), 57 (5.3). IR (KBr, cm^{-1}): ν O–H 3450 (broad), 3419 and 3450 cm^{-1}, ν C–H 3136 (CH=N), ν C–H 3087 (aromatic), ν_{as} –CH_3 2955, ν_s –CH_3 2863, ν –C=N 1623, ν_{as} –NO_2 1535, ν_s –NO_2 1342. ^{1}H NMR (400 MHz) ($CDCl_3$, δ, ppm): 1.40 (s, 9H, *t*Bu-H); 6.41 (s, 1H, H-9); 6.93–6.99 (m, 2H, H-28 and H-32); 7.38–7.42 (m, 2H, H-34 and H-30); 7.61 (t, 1H, 3 J = 7.8 Hz, H-16); 7.72 (d, 1H, 3 J = 7.6 Hz, H-13), 7.79 (t, 1H, 3 J = 7.4 Hz, H-20); 8.04 (*d*, 1H, 3 J = 8.0 Hz, H-18); 8.75 (*s*, 1H, H-22); 11.68 (bs, 1H, OH). ^{13}C NMR (100 MHz) ($CDCl_3$, δ, ppm) 30.28 (*t*Bu-C); 32.77 (C-35); 90.30 (C-8); 117.33 (C-27), 118.75 (C-23); 119.69 (C-31); 125.29 (C-17); 129.22 (C-12); 129.23 (C-15); 132.13 (C-11); 132.96 (C-33); 133.21 (C-19); 134.18 (C-29); 146.08 (C-14); 148.82 (C-10); 160.69 (C-24); 163.24 (C-21); 164.34 (C-7).

(E)−2-(((3-(tert−butyl)−1-(3-nitrophenyl)−1H-pyrazol-5-yl)imino)methyl)phenol ***2b***

Yellow solid. M.p. 147–148 °C. Anal. calcd. %C 65.92; %H 5.53; %N 15.38, found: %C 65.98; %H 5.64; %N 15.42, for $C_{20}H_{20}N_4O_3$ MS (70 eV) *m/z* (%) 364 $[M]^+$ (100), 349 $[M-15]^+$ (51.95), 318 $[M-46]^+$ (16), 307 $[M-57]^+$ (1.37) 122 (1.64), 57 (5.29). IR (KBr, cm^{-1}): ν O–H 3419 (broad), ν C–H 3126 (CH=N), ν C–H 3095 (aromatic), ν_{as} $-CH_3$ 2968, ν_s $-CH_3$ 2863, –C=N, 1623, ν_{as} $-NO_2$ 1526, ν_s $-NO_2$ 1347. ^{1}H NMR (400 MHz) ($CDCl_3$, δ, ppm): 1.44 (s, 9H, *t*Bu-H); 6.41 (s, 1H, H-9); 6.99–7.02 (m, 2H, H-28 and H-32); 7.42–7.46 (m, 2H, H-30 and H-34); 7.69 (t, 1H, 3 J = 8.1 Hz, H-18); 8.01 (d, 1H, 3 J = 7.8 Hz, H-20); 8.24 (d, 1H, 3 J = 8.1 Hz, H-16); 8.58 (s, 1H, H-13); 8.80 (s, 1H, H-22); 11.85 (bs, 1H, OH). ^{13}C NMR (100 MHz) ($CDCl_3$, δ, ppm) 30.30 (*t*Bu-C); 32.73 (C-35); 91.36 (C-8); 117.50 (C-27); 118.73 (C-23); 119.58 (C-31); 119.77 (C-12); 121.77 (C-15); 129.82 (C-17); 129.84 (C-19); 132.97 (C-33); 134.41 (C-29); 140.03 (C-11); 148.18 (C-10); 148.71 (C-14); 160.81 (C-24); 163.46 (C-21); 163.75 (C-7).

(E)−2-(((3-(tert−butyl)−1-(4-nitrophenyl)−1H-pyrazol-5-yl)imino)methyl) ***2c***

Yellow solid. M.p. 204–205 °C. Anal. calcd. %C 65.92; %H 5.53; %N 15.38, found: %C 66.03; %H 5.57; %N 15.27 for $C_{20}H_{20}N_4O_3$. MS (70 eV) *m/z* (%) 364 $[M]^+$ (100), 349 [M 15]$^+$ (71.7), 318 $[M-46]^+$ (1.4), 307 $[M-57]^+$ (2.13), 122 (1.84), 57 (12.97). IR (KBr, cm^{-1}): ν O–H 3450 (extremely broad), ν C–H 3135 (CH=N), ν C–H 3087 (aromatic), ν_{as} $-CH_3$ 2954.56, ν_s $-CH_3$ 2862, ν –C=N 1623, ν_{as} $-NO_2$ 1519, ν_s $-NO_2$ 1342. ^{1}H NMR (400 MHz) ($CDCl_3$, δ, ppm): 1.43(s, 9H, *t*Bu-H); 6.41 (s, 1H, H-9); 7.01–7.04 (m, 2H, H-28 and H-32); 7.44–7.48 (m, 2H, H-34 and H-30); 7.90 (d, 2H, 3 J = 9.1 Hz, H-16 and H-13); 8.39 (d, 2H, 3 J = 9.1 Hz, H-20 and H-18); 8.80 (s, 1H, H-22); 11.92 (bs, 1H, OH). ^{13}C NMR (100 MHz) ($CDCl_3$, δ, ppm) 30.22 (*t*Bu-C); 32.77 (C-35); 92.17 (C-8); 117.51 (C-27); 118.70 (C-23); 119.87 (C-31); 123.95 (C-15 and C-12); 124.71 (C-19 and C-17); 133.05 (C-29); 134.58 (C-33); 144.13 (C-11); 145.87 (C-14); 148.51 (C-10); 160.79 (C-24); 163.67 (C-21); 164.10 (C-7).

2.3. Computational study

Density Functional Theory (DFT) computational methods B3LYP [30] with the basis set 6–311++G^{**} and Gaussian packet 09 [31] were used. Vibration frequencies were interpreted by means of potential energy distributions (PEDs), using the VEDA 4 program [32] and the percentage contribution of the frontier orbitals at each transition of electronic absorption spectrum using GaussSum software [33].

2.4. X-ray diffraction crystallography

Single-crystals suitable for X-ray diffraction were obtained for Schiff bases **2b** (slow evaporation of acetone solution) and **2c** (slow evaporation of dichloromethane solution). Data for compound **2b** were collected at room temperature (298 K) on a Bruker Apex-II CCD diffractometer using monochromatic graphite MoKα (0.71073Å) radiation. Cell determination and final cell parameters were obtained on all reflections using the Bruker SAINT software included in APEX2 software suite. The integration and scaling of the data were carried out using the Bruker SAINT software. Data collection for compound **2c** was performed at room temperature on a Bruker APEX-II CCD diffractometer with CCD detector system equipped with a Mo source (λ = 0.71073 Å). Data integration, Lorentz-polarization effects, and absorption corrections were performed with CrysAlisPro [34]. Using the Olex2 program [35], the structures were solved by direct methods and the models obtained were refined by full–matrix least squares on F2 (SHELXTL–97) [36]. All the hydrogen atoms were placed in calculated positions and refined with fixed individual displacement parameters [Uiso(H) = 1.2Ueq or 1.5Ueq] according to the riding model (C–H bond lengths of 0.93 Å and 0.96 Å, for methyl and aromatic hydrogen, respectively). To the exception of the hydrogen atom of the hydroxyl group, this was located from the electronic density. Molecular representations were generated by Diamond [37] and MERCURY 3.9 [38]. The CIF files have been deposited in the Cambridge Structural Data Base [39] under the codes CCDC 1864392 for **2b** and 1864393 for **2c**. Copies of the data can be obtained, free of charge, at www.ccdc.cam.ac.uk.

2.5. Antifungal activity

The antifungal activity was determined using the standardized microbroth dilution method M-27A3 of Clinical and Laboratory Standards Institute (CLSI) [40]. Compounds **2a-c** were tested against two clinically important fungal species, *C. albicans* ATCC 10231 and *C. neoformans* ATCC 32264, from the American Type Culture Collection, (ATCC, Rockville, MD, USA). Inocula of cells were adjusted to 1 - 5 $\times$ 10^3 cells with colony forming units (CFU)/mL according to CLSI [40].

2.5.1. Fungal growth inhibition percentage determination

Broth microdilution techniques were performed in 96-well microplates according to the CLSI Reference Method for Broth Dilution Antifungal Susceptibility Testing of Yeasts, Approved Standard M27-A3 [40]. Compound test wells (CTWs) were prepared with stock solutions of each compound in DMSO (maximum concentration $\leq$ 1%), diluted with RPMI-1640, to final concentrations of 250–3.4 μg/mL. An inoculum suspension (100 mL) was added to each well (final volume in the well = 200 μL). A growth control well (GCW) containing medium, inoculum, and the same amount of DMSO used in a CTW, but compound-free and a sterility control well (SCW) (sample, medium, and sterile water instead of inoculum) were included for each tested fungus. Microtiter trays were incubated in a moist, dark chamber at 30 °C for 48 h. Microplates were read in a VERSA Max microplate reader (Molecular Devices, Sunnyvale, CA, EE: UU). Amphotericin B (Sigma-Aldrich) was used as a positive control. Tests were performed in triplicate. Reduction of growth for each compound concentration was calculated as follows: % of inhibition = 100 - (OD 405 CTW - OD 405 SCW)/(OD 405 GCW - OD 405 SCW). The means $\pm$ SEM were used for constructing the dose-response curves representing % inhibition *vs* concentration of each compound using SigmaPlot 11.0 software.

2.5.2. Determination of minimum inhibitory concentration (MIC)

Three endpoints were defined from the dose-response curves. The concentration resulting in total fungal growth inhibition was named MIC_{100}, while MIC_{80} and MIC_{50} were defined as the minimum concentration that inhibits 80% or 50% of the fungal growth, respectively.

2.6. Molecular docking calculations

The study was developed in the software AutoDock Vina 1.1.2 [41] and ADT 1.5.6 [42]. To determine the dimensions of the box in the active site of the protein, studies based on the literature were taken as reference [43]. The dimension of the mesh box was 1 Å, with an exhaustiveness value of 15 and the binder-macromolecule interactions were visualized using BIOVIA Discovery Studio [44]. The crystal structures of the *Saps* and *Hsp90* proteins were downloaded from the protein data bank (PDB ID: 3PVK and 2XJX respectively). In both cases, water molecules were removed from the protein and the polar hydrogens were added along with the Gasteiger charges. Structures of compounds **2a-c** previously optimized by DFT were saved in PDB format using the Avogadro software [45]. Polar hydrogen atoms and Gasteiger charges were added.

Table 1
Yields (%) obtained for compounds **2a-c** using different reaction conditions.

Compound	Conventional synthesis[a]	Fusion[b]	Microwave assisted[c]	Mechano chemistry[d]
2a	68	95	96	84
2b	86	98	98	94
2c	72	98	98	94

[a] Ethanol reflux, stirring for 24 h.
[b] Neat, 160 °C for 1 h.
[c] Ethanol, 100 W, 3 × 5 min.
[d] Neat, room temperature, grinding for 20 min.

Table 2
Crystallographic data and refinement parameters for Schiff bases **2b** and **2c**.

Compound	2b	2c
Emp. Formula	C_{20} H_{20} N_4 O_3	C_{20} H_{20} N_4 O_3
FW (g•mol^{-1})	364.40	364.40
Temp. (K)	293 (2)	293 (2)
λ (Å)	0.71073	0.71073
Crystal system	Orthorhombic	Monoclinic
Space Group	P*na*2_1	C2/c
a **(Å)**	8.7683(4)	10.2224(5)
b **(Å)**	22.7334(10)	20.6591(9)
c **(Å)**	9.5633(5)	18.6509(10)
β **(°)**	90	104.246(5)
Volume (Å^3)	1906.28(16)	3817.7(3)
Z	4	8
ρ_{calc} (mg•m^3)	1.270	1.268
Abs. Coeff. (mm^{-1})	0.088	0.088
F(000)	768	1536
θ **range (°)**	1.8 to 26.4	3.5 to 27.5
Reflections collected / Unique	57,163/3901	24,006/4345
[R(int)]	[0.051]	[0.027]
Completeness (%)	100	99.3
Data / restraints / parameters	3901/0/273	4345/0/252
GoF on F^2	1.05	1.04
R1 [*I*>2*σ*(I)]	0.0488	0.0672
wR2[*I*>2*σ*(I)]	0.1303	0.1820

3. Results and discussion

3.1. Synthesis and characterization

Compounds **2a, 2b**, and **2c** bearing a 2-, 3- or 4-nitrophenyl substituent were synthesized by condensation of amines **1a, 1b** and **1c and** 2-hydroxybenzaldehyde through various methods such as fusion, conventional heating in solution, microwave-assisted synthesis and mechanochemistry (Scheme 1). The best results were obtained through the solvent-free approach or using a microwave reactor, obtaining almost quantitative yields in both cases. Yields obtained through the different techniques are summarized in Table 1. The structure of the compounds was confirmed by FT-IR, ^{1}H and ^{13}C NMR, MS and X-ray diffraction crystallography and their purity assessed by elemental analysis.

3.2. Crystallography

The crystallographic data and refinement details are presented in Table 2, and ORTEP representations of **2b** and **2c** are displayed in Fig. 1.

The two compounds crystallized in different systems. Schiff base **2b** crystallized in the non-centrosymmetric P*na*2_1 orthorhombic space group with one molecule in the asymmetric unit. On the other hand, Schiff base **2c** crystallized in C2/c monoclinic space group with one molecule in the asymmetric unit. Interestingly, these two compounds present marked differences associated with the torsion angles in the connection of the phenol and nitrophenyl rings to the pyrazolic structure. In the first case, torsion angles for N4-N3-C11-C16 of 33.82 and 39.64° are observed, for **2b** and **2c**, respectively. In the case of the torsion angle associated with the imine and phenol ring N1-C7-C6-C1, values of 0.48° and −0.13° are observed for **2b** and **2c**, respectively (Fig. 2). These differences are related to the position of the nitro group, and the crystal packing produced by those particular interactions. In both structures, a positional disorder around the *tert*–butyl group is observed.

The supramolecular crystal packing for compounds **2b** and **2c** is based in weak C–H•••O and C–H•••C interactions. For compound **2b**, a C9–H9•••O2 interaction with a distance of 3.507 Å is observed, forming chains along [001] direction (Fig. 3a). The chains are stacked along [010] direction by C16–H16•••C12 interactions with a distance of 3.726 Å (Fig. 3b). The crystal packing is based in C–H•••C and H•••H interactions along of [100] (Fig. 3c).

Compound **2c** presents C9–H9•••O2 and C7–H7•••O2 interactions with distance values of 3.427 and 3.545 Å, which give rise to chains along [010] direction (Fig. 4a). The chains are joined by C19–H19•••O3 interaction with a distance of 3.321 Å along [001] direction (Fig. 4b). As observed for **2b**, the 3D supramolecular structure is formed by weak C–H•••C and H•••H interactions (Fig. 4c).

3.3. Vibrational analysis

Experimental and theoretical IR spectra of compounds **2a-c** are presented in Figure S1 and the vibration frequencies are summarized in Table S1. The theoretical frequencies and intensities were calculated via the B3LYP method. The scale factor for the method was 0.960461 DFT-B3LYP/6–311++*G*** [19,46–48]. The correlation coefficients R^2 (0.9993 for **2a**, 0.9982 for **2b** and 0.9989 for **2c**), were obtained from the linear correlation curves between the calculated and experimental data (Figure S2). The experimental vibration of the hydroxyl group is observed as a broad band of a very low intensity at 3450, 3419 and 3450 cm^{-1} for compounds **2a, 2b** and **2c** respectively, which is attributed to the formation of a strong intramolecular bond between the hydrogen of the hydroxyl group and the nitrogen of the azomethine functionality [19,49–51]. Calculated values are obtained at 3206, 3202 and 3212 cm^{-1} for **2a, 2b** and **2c**, respectively, with significant increased intensities, indicating that the strong intramolecular OH•••N=C hydrogen bonding was not considered in the calculations. Interestingly, the experimental vibrational frequencies for the C=N bonds are observed at 1623 cm^{-1} for the three Schiff bases **2a-c**. This phenomenon is also observed for the theoretical C21–N5 bond distances, in agreement with the experimental data obtained from the resolved crystalline structures for **2b** and **2c** (Table 1). This property is associated with the interaction between the phenolic hydrogen and the azomethinic nitrogen forming the same stable hydrogen bonds in all three structures [19,52,53]. Moreover, no effect of the position of the nitro group is observed because it is too far from the C21–N5 azomethine bond.

3.4. NMR studies

^{1}H and ^{13}C NMR spectra of compounds **2a-c** are shown in Figure S3-S5 and Figure S6-S8 respectively. The singlet located at 1.40, 1.44 and 1.43 ppm is assigned to the nine protons of the *tert*–butyl group in **2a, 2b** and **2c**. The singlet located at 6.41 ppm (in all three compounds) is assigned to the pyrazole proton (H-4). The singlet signal assigned to the proton of the imine group (H-15) is observed at 8.75, 8.80 and 8.80 ppm for **2a, 2b** and **2c** respectively. Additionally, as expected the azomethine proton (H-15) in **2b** and **2c** is displaced to lower field in comparison with the azomethine hydrogen in **2a** due to the deactivating effect of the nitro group [19–21]. Finally, the singlet signal located at 11.68, 11.85 and 11.92 ppm is assigned to the hydroxyl proton for **2a, 2b**

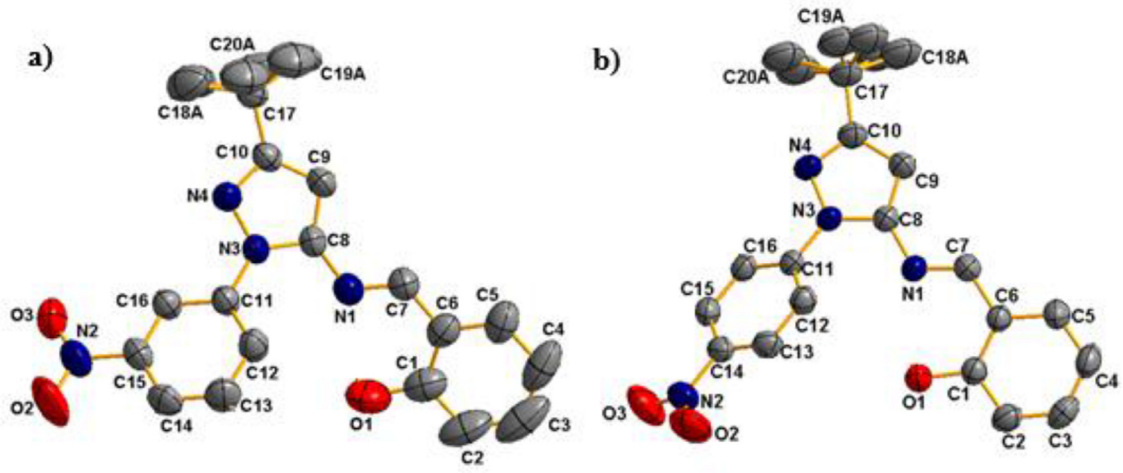

Fig. 1. ORTEP diagram of the asymmetric unit of compounds **2b** (a) and **2c** (b) at 50% of probability. Hydrogen atoms are omitted for clarity.

and **2c**. In the ^{13}C NMR, the different chemical shifts of the aromatic carbons are due to the deactivating effect of the nitro group, where the carbon atoms in *ortho* and *para* to the nitro group are displaced at lower field. The signal observed at 160.62, 160.81 and 160.79 ppm is assigned to imine group (C-15) in **2a, 2b** and **2c**. Again, these differences are caused by the electron-withdrawing effect of the nitro group.

3.5. DFT optimization and frontier molecular orbitals

The optimization of the geometries for the three Schiff bases **2a-c** in their ground states was carried out using the B3LYP level with the basis set 6–311++G^{**}. Optimized structures are presented in Figure S13. Table S2 shows values for the calculated bond angles, bond lengths and dihedral angles, in addition to the experimental data for compounds **2b** and **2c**. Only limited differences can be observed between the calculated dihedral angles, bond angles and lengths and those determined experimentally. Noteworthy, the intermolecular interactions NO•••H and CH•••O and the intra-molecular interactions OH•••N that arise during the crystal packing and the nitro-substitution in the aromatic ring affect the crystal structure of compounds **2a, 2b** and **2c**, and therefore are likely to be responsible for the small differences noted between the theoretical and experimental data [46]. The calculated data for the C21–N5 imine bonds show that they are not affected by the position of the nitro group, displaying a bond length of 1.294 Å in all three cases. However, the experimental data show that the C21–N5 bond is longer in **2c** than in **2b**. This discrepancy is possibly caused by intramolecular N•••H interactions not considered in the theoretical calculations. Fig. 5 shows the molecular orbitals (MOs) distributions of the HOMO and LUMO for compounds **2a-c**. The HOMO to LUMO band gap energy is 3.302, 3.188 and 3.279 eV for **2a, 2b** and **2c**, indicating that **2b** is the most reactive, implying lower kinetic stability and higher chemical reactivity [54]. Noteworthy, in all three compounds, the HOMO orbital is delocalized over the azomethine moiety, pyrazole ring and phenol. The LUMO orbital for **2a** and **2b** is located in the nitrophenyl moiety, while for **2c** it is mainly localized on the nitrophenyl moiety with a contribution of the pyrazole ring [55,56].

3.6. Molecular electrostatic potential (MEP) and global reactivity descriptors

MEP map has been used to visualize the different charged regions of a molecule and has proven to be a useful tool to study

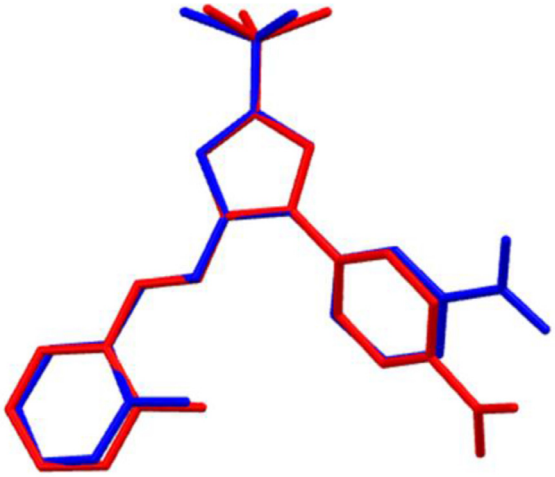

Fig. 2. Superimposed structures of Schiff base **2b** (blue) and Schiff base **2c** (red).

the structure-activity relationship [57,58]. Calculations show that in **2a-c** the negative electrostatic potential is mainly located on the oxygen atoms of the nitro and hydroxyl group and on the nitrogen of the pyrazole moiety, these being the reactive sites for an electrophilic attack, while the positive electrostatic potential (blue regions) is localized over the C–H bonds of the compounds, thereby these electron-poor sites have affinity towards nucleophiles (Fig. 6) [59].

Global reactivity parameters were also calculated and data in Table 3 confirm that compound **2b** is the most reactive of the series [60,61]. In order to evaluate the effect of the nitro-group on

Table 3
Calculated HOMO–LUMO energies and global reactivity parameters for compounds **PhPzSal** and **2a**-**c**.

Parameters	PhPzSal [21]	2a	2b	2c
E_{HOMO}	−6.155	−6.360	−6.303	−6.375
E_{LUMO}	−2.375	−3.058	−3.115	−3.096
ΔE_{HOMO} -ΔE_{LUMO}	3.780	3.302	3.188	3.279
Electronegativity (χ)	4.265	4.709	4.709	4.736
Chemical hardness (η)	1.890	1.651	1.594	1.640
Global softness (σ)	0.529	0.606	0.627	0.610
Chemical potential (μ)	−4.265	−4.709	−4.709	−4.736
Electrophilicity index (ω)	4.812	6.716	6.956	6.839

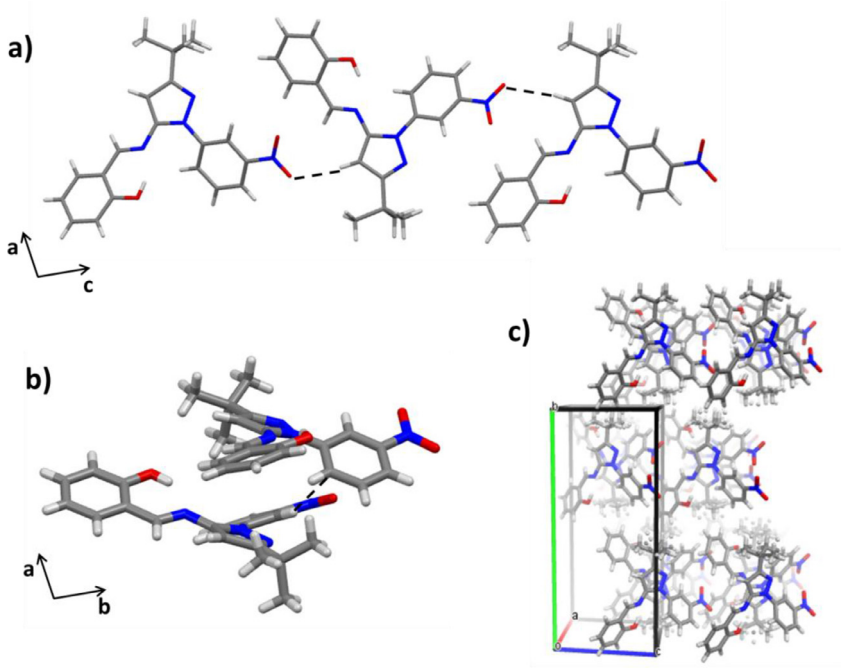

Fig. 3. Interactions along [001] direction (a), C–H•••C interactions (b) and crystal packing (c) for compound **2b**.

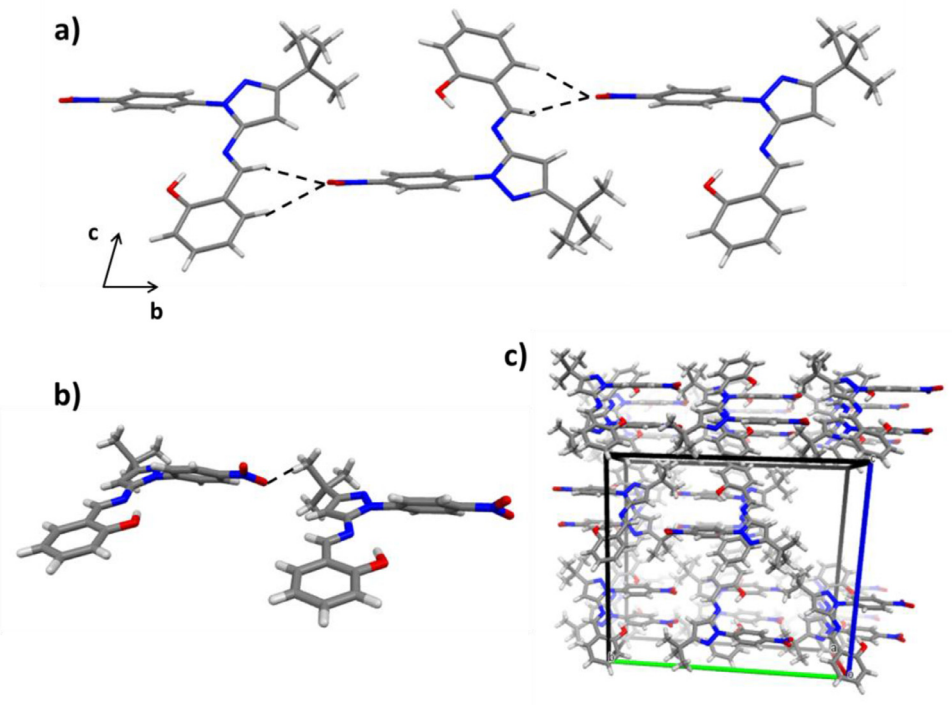

Fig. 4. Interactions along [010] direction (a), C–H•••O interactions (b) and crystal packing (c) for compound **2c**.

the different parameters, data for the previously reported unsubstituted **PhPzSal** compound (see structure in Figure S14) have been included [21]. Schiff base **PhPzSal** presents the lowest ionization potential (IP) value, which makes it a good electron donor. Compound **2b** presents the highest values for the electronic affinity (EA) and electrophilicity (ω) which makes it a better electrophile than **PhPzSal, 2a** and **2c**. Another parameter of great importance is the softness (σ) and the hardness (η). Derivative **2b** presents the highest value of softness and the lowest value of hardness, corroborating that this compound has the highest electrophilic character, and as such the most reactive compound in this series of Schiff bases.

3.7. Antifungal activity

The next step of our study was to evaluate the antifungal activity of the compounds. *C. albicans* and *C. neoformans* fungi were chosen due to the importance of these species in the epidemiology of fungal infections. *C. albicans* is among the leading causes of bloodstream infections worldwide [62,63], and *C. neoformans*

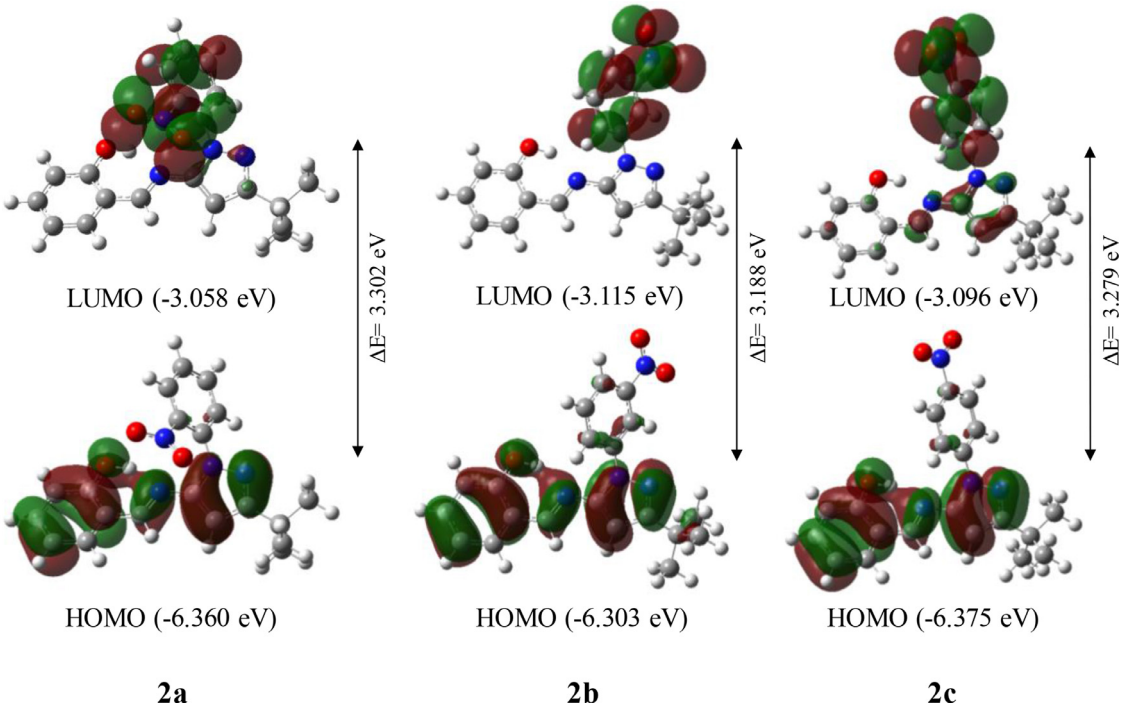

Fig. 5. Comparison of HOMO\LUMO energies for the different Schiff bases.

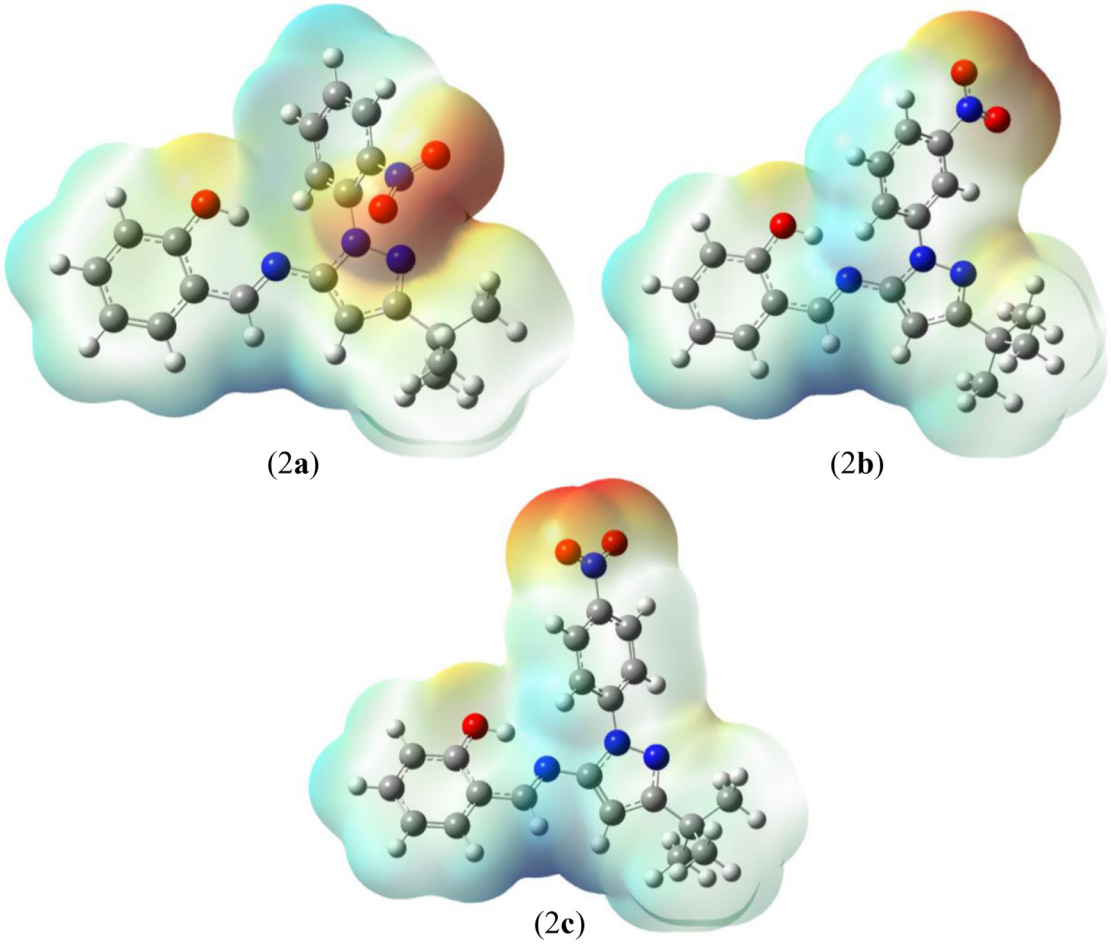

Fig. 6. Electrostatic potential surface for the Schiff bases at DFT/B3LYP level. The red and blue regions represent the most negative and most positive potentials while the green one represents the zero potential.

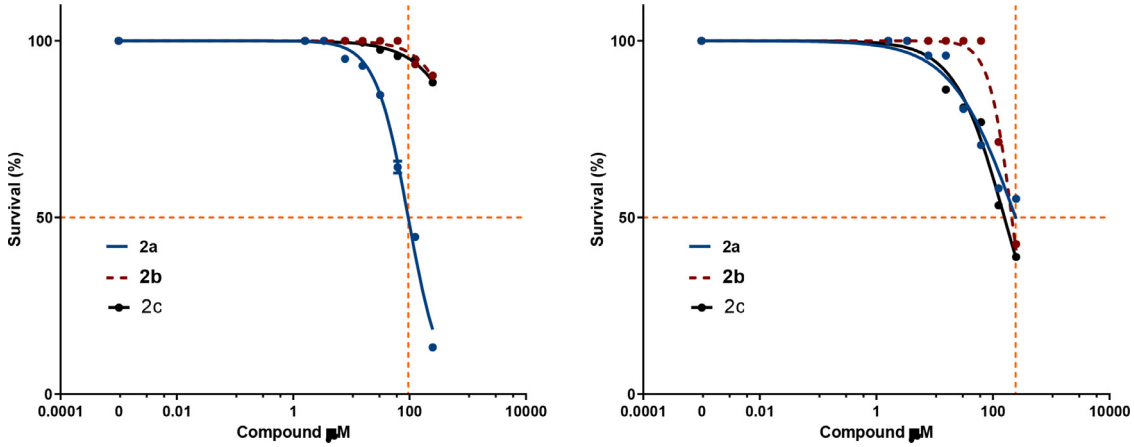

Fig. 7. Dose-response curves of compounds **2a-c** *C. albicans* ATCC 10231 (left) and *C. neoformans* ATCC 32264 (right). Compounds test wells were prepared with stock solutions of each compound in DMSO. Microtiter trays were incubated in a moist, dark chamber at 30 °C for 48 h.

remains a life-threatening complication for immunocompromised hosts. *C. neoformans* is considered as the leading cause of cryptococcal meningoencephalitis generating a high mortality rate among patients with profoundly altered infections, particularly patients suffering from HIV [64,65]. Table S3 shows the antifungal results expressed as a percentage of inhibition of each fungal growth in the range of 250–3.4 μg/mL, together with the minimum concentration of the **2a-c** compounds that inhibited 100, 80 or 50% of the growth of both fungi (MIC_{100}, MIC_{80} and MIC_{50}). Fig. 7 shows the dose-response curves against each fungus. Compound **2a** displayed a much higher activity that **2b** and **2c** against *C. albicans* with a 50% inhibition of growth at a concentration of 125 μg/mL at 48 h incubation time. In contrast, all three derivatives showed a comparable activity against *C. neoformans* with **2c** being slightly more active, with a 61% of inhibition of growth at a concentration of 250 μg/mL at 48 h incubation time.

In an attempt to rationalize such results, the calculated reactivity parameters (Table 2) were compared for the **2a-c** series. Compound **2a** presents the highest values of chemical hardness, indicating a slightly higher electrophilicity than **2b** and **2c**. This may indicate that the specific proteins of *C. albicans* tend to interact with electrophilic compounds.

3.8. Molecular docking studies and LigPlot analysis

To gain a better understanding on the differences observed in the antifungal activity and the influence of the position of the nitro group, molecular docking calculations were performed. Considering the importance of the metabolic functions of the Saps and Hsp90 proteins in fungal microorganisms, these were chosen as targets. The secreted aspartic protein (Saps) was selected as it plays an important role in the infection process and is responsible for virulence. Adhesion and tissue damage are attributed to the Saps protein, and therefore, can be considered a valuable inhibition target for *C. albicans* [66]. The Hsp90 protein or chaperone protein was selected as it is present in the cell transduction and signaling. The main function of Hsp90 is observed in the process of virulence and drug resistance. Hence, the inhibition of the Hps90 protein is an attractive target for the treatment of fungal diseases caused by *C. neoformans* [67]. To generate a valid procedure, the optimized ligand is self-docking in triplicate in the active site of the protein [PDB ID: 3PVK] for *C. albicans* and [PDB ID 2XJX] for *C. neoformans*. Calculations using the optimized structures for compounds **2a-c** reveal that they present interactions in the active site of the proteins in the -6.33 ± 0.047 to -7.47 ± 0.120 kcal/mol range (Table 4).

Table 4
Binding energy of compounds **2a-c** on molecular targets in *C. albicans* and *C. neoformans* after molecular docking calculations.

	Protein	
	3PVK Energy ΔE (kcal/mol)	2XJX Energy ΔE (kcal/mol)
Compound	$\bar{X} \pm$ SD	$\bar{X} \pm$ SD
2a	-6.33 ± 0.047	-6.63 ± 0.047
2b	-6.97 ± 0.047	-7.47 ± 0.120
2c	-7.03 ± 0.009	-6.60 ± 0.210

According to the data shown in Table 3, the 3PVK protein presents a higher affinity towards the **2c** binder, with an energy value of -7.03 ± 0.009 kcal/mol, while the 2XJX protein shows a higher affinity towards compound **2b** with an energy value of -7.47 ± 0.120 kcal/mol. This agrees with the data obtained for the reactivity parameters shown in Table 2, where compounds **2c** and **2b** display the lowest values of chemical hardness, indicating that these compounds tend to easily donate electronic density and thus improving binding to proteins. Interestingly, the most active compound (**2a**) against *C. albicans* presents the lowest binding energy with 3PVK protein. Fig. 8 and S15 show the binding modes between compounds **2a-c** and the 3PVK and 2XJX proteins respectively.

Table S4 summarizes the different interactions and binding affinities between **2a-c** and 3PVK and 2XJX. Hydrophobic interactions and hydrogen bonds between the **2a-c** binders and the 3PVK and 2XJX proteins are highlighted in the LigPlot diagrams in Fig. 9 and S16 respectively. Compound **2c** presents nine hydrophobic interactions with the 3PVK protein and four hydrogen bonding interactions of which, two interactions of oxygen 1 (O1) with amino acids Thr222 and Tyr225, one interaction of oxygen 3 (O3) with amino acid Gly220 and one interaction of nitrogen 3 (N3) with the amino acid Thr221 as can be seen in Table S4. On the other hand, compound **2b** presents two hydrogen bonding interactions of oxygen 1 (O1) with amino acid Thr222 and of oxygen 3 (O3) with amino acid Gly220. According to the calculated bonding energies interactions of compounds **2a-c** with the 2XJX protein, compound **2c** shows stronger interaction than compounds **2a** and **2b** (Table S4). LigPlot analysis showed that hydrogen binding with the nitro group takes place in all cases, providing a stable position near key residues of 3PVK protein (Fig. 9). Notably, compound **2c** displays four hydrogen bonds with residues Gly220, Thr221, Thr222 and Ile223. The nitro group in this case is involved in two hydrogen bonds with residues 222 and 223. The nitro group is in *para*

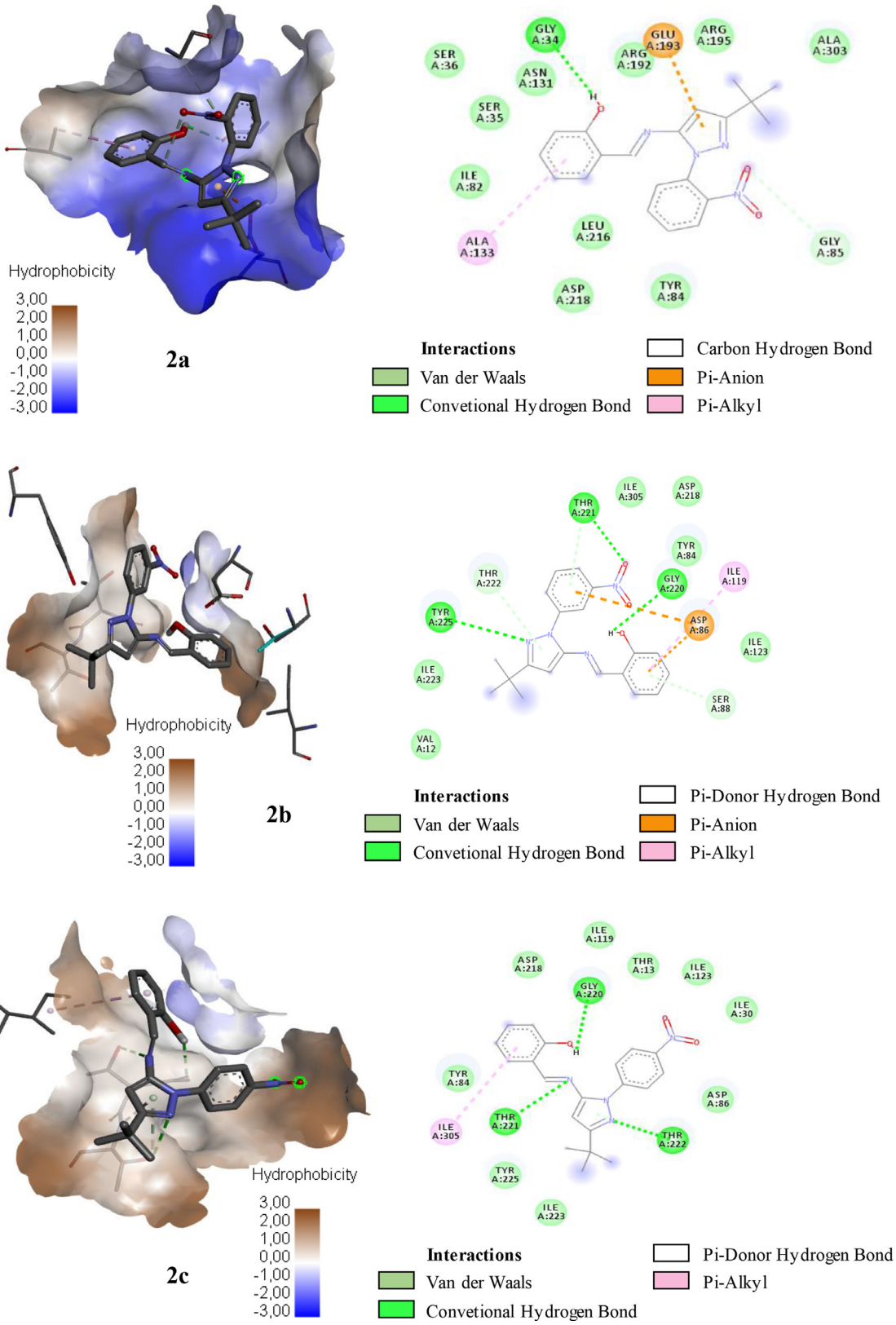

Fig. 8. Binding modes of co-crystalized compounds **2a-c** with 3PVK protein.

position in compound **2c**, which should allow it to be more exposed to these residues. In case of **2a**, only a single hydrogen bond is involved, this is most likely because the phenyl ring is *ortho* substituted with the nitro group and therefore is more hindered. These three different positions for compounds **2a-c** are stabilized by hydrophobic C–H π interactions with the phenyl rings in the molecule. The ability of a nitro group to delocalize positive charge in aromatic rings showed no important effect in the protein-ligand interactions. However, torsion can explain how a conformation is preferred among others [68]. For the nitro group in *ortho* posi-

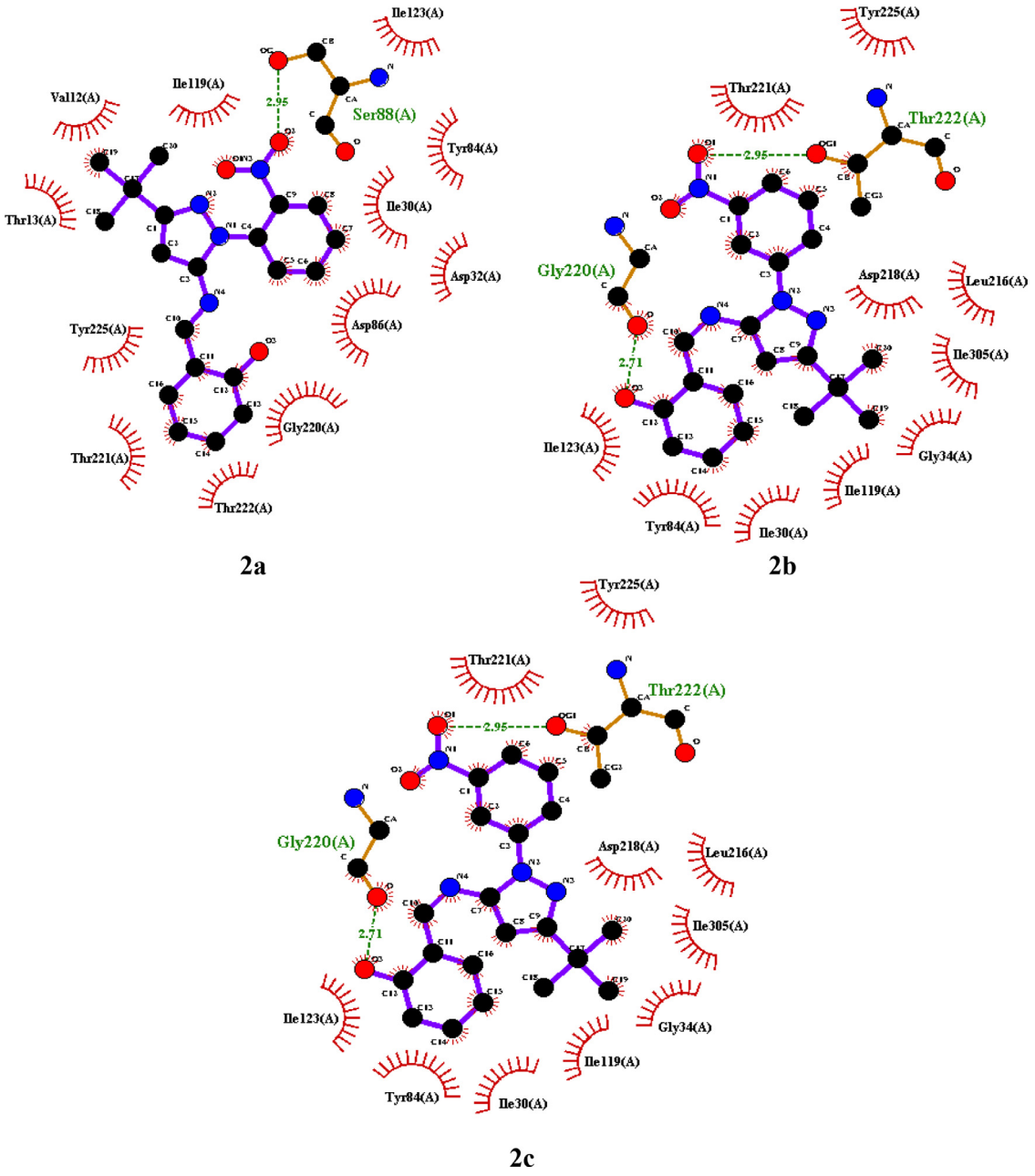

Fig. 9. LigPlot analysis of intermolecular interactions between compounds **2a-c** and the 3PVK protein. Green lines indicate the hydrogen bonds and red dotted lines indicate the hydrophobic interactions. (For interpretation of the references to color in this figure legend, the reader is referred to the web version of this article.)

tion (**2a**), the torsion angle between the phenyl ring and one of the oxygen atoms is −41.52° which indicates that the nitro group is hindered, while *meta* substitution (**2b**) shows a torsion angle of 179.46° and for *para* substitution (**2c**) a torsion angle of −179.50° is observed. Both compounds with *meta* and *para* are close in energy but compound **2c** with the nitro group in *para* position shows a slightly better affinity to the 3PVK protein due to more hydrogen bonds, possibly because the negative torsion angle directs the oxygen atom towards Thr222 and Ile223 residues.

4. Conclusions

In summary, the synthesis of three azomethine isomers (**2a-c**) based on a pyrazole moiety substituted by a nitrophenyl group was studied using different methodologies, obtaining the best yields through environmentally friendly techniques. Theoretical DFT calculations show that **2b** displays the smallest HOMO-LUMO energy gap and the highest value of softness, corroborating that this compound has the highest electrophilic character and is the most reactive within this series of Schiff bases. Antifungal studies on *C. albicans* clearly show that the position of the nitro group has a considerable impact on the activity, while on *C. neoformans*, the influence is much less important. Molecular docking studies showed that the most biologically active compound (**2a**) against *C. albicans* presents the lowest affinity with model 3PVK protein, and the differences in antifungal activity observed between the 3 isomers, are more likely be a consequence of steric considerations rather than electronic effects caused by the nitrophenyl substituent. However, no definite explanation on the exact role of the nitro group on the antifungal activity can be drawn at this stage of the work, and further investigation is needed to establish the possible mechanisms of action.

Declaration of Competing Interest

The authors declare that they have no known competing financial interests or personal relationships that could have appeared to influence the work reported in this paper.

CRediT authorship contribution statement

Andrés Restrepo-Acevedo: Formal analysis, Data curation, Writing – original draft. **Nicolas Osorio:** Formal analysis, Data curation, Writing – original draft. **Luis E. Giraldo-López:** Formal analysis, Data curation, Writing – original draft. **Richard F. D'Vries:** Formal analysis. **Susana Zacchino:** Formal analysis, Data curation. **Rodrigo Abonia:** Formal analysis, Data curation. **Ronan Le Lagadec:** Validation, Writing – review & editing. **Fernando Cuenú-Cabezas:** Conceptualization, Formal analysis, Resources, Writing – review & editing, Visualization, Supervision.

Acknowledgement

Total financial support from the Vice-Rectory of Research (Projects 789 and 920) at Universidad del Quindío (Armenia, Colombia) is gratefully acknowledged. R.D. acknowledges the Dirección General de Investigaciones from Universidad Santiago de Cali. Dr. J. A. Solís-Ruiz is thanked for helpful discussions.

Supplementary materials

Supplementary material associated with this article can be found, in the online version, at doi:10.1016/j.molstruc.2021.132289.

References

[1] A.A. Shanty, P.V. Mohanan, Heterocyclic Schiff bases as non-toxic antioxidants: solvent effect, structure activity relationship and mechanism of action, Spectrochim. Acta. A. 192 (2018) 181–187, doi:10.1016/j.saa.2017.11.019.
[2] M.A. Pfaller, D.J. Diekema, are and Emerging Opportunistic Fungal Pathogens: concern for resistance beyond *Candida albicans* and *Aspergillus fumigatus*, J. Clin. Microbiol. 42 (2004) 4419–4431, doi:10.1128/JCM.42.10.4419-4431.2004.
[3] D. Olender, J. Żwawiak, L. Zaprutko, Multidirectional efficacy of biologically active nitro compounds included in medicines, Pharma 11 (2018) 1–29, doi:10.3390/ph11020054.
[4] M. Taneda, K. Amimoto, H. Koyama, T. Kawato, Photochromism of polymorphic 4,4′-methylenebis(*N*-salicylidene-2,6-diisopropylaniline) crystals, Org. Biomol. Chem. 2 (2004) 499–504, doi:10.1039/b311669g.
[5] M. Sliwa, S. Letard, I. Malfant, M. Nierlich, P.G. Lacroix, T. Asahi, H. Masuhara, P. Yu, K. Nakatani, Synthesis, structural and nonlinear optical properties of photochromic crystals: toward reversible molecular switches, Chem. Mater. 17 (2005) 4727–4735, doi:10.1021/cm050929o.
[6] K. Rustler, P. Nitschke, S. Zahnbrecher, J. Zach, S. Crespi, B. König, Photochromic evaluation of 3(5)-arylazo-1*H*-pyrazoles, J. Org. Chem. 85 (2020) 4079–4088, doi:10.1021/acs.joc.9b03097.
[7] K. Takahashi, Y. Hasegawa, R. Sakamoto, M. Nishikawa, S. Kume, E. Nishibori, H. Nishihara, Solid-State Ligand-Driven Light-Induced Spin Change at Ambient Temperatures in bis(dipyrazolylstyrylpyridine)iron(II) Complexes, Inorg. Chem. 51 (2012) 5188–5199, doi:10.1021/ic300030b.
[8] W.M.F. Fabian, L. Antonov, D. Nedeltcheva, F.S. Kamounah, P.J. Taylor, Tautomerism in hydroxynaphthaldehyde anils and azo analogues: a combined experimental and computational study, J. Phys. Chem. A. 108 (2004) 7603–7612, doi:10.1021/jp048035z.
[9] E.N. Shepelenko, A.V. Tsukanov, Yu.V. Revinskii, A.D. Dubonosov, V.A. Bren, V.I. Minkin, Benzoid-quinoid tautomerism of Schiff bases and their structural analogs: LIII. Schiff bases derived from 5-hydroxy- and 5-hydroxy-6-nitro-2,3-diphenyl-1-benzofuran-4-carbaldehydes, Russ. J. Org. Chem. 43 (2007) 559–563, doi:10.1134/S1070428007040124.
[10] T. Dziembowska, E. Jagodzinska, Z. Rozwadowski, M. Kotfica, Solvent effect on intramolecular proton transfer equilibrium in some *N*-(R-salicylidene)-alkylamines, J. Mol. Struct. 598 (2001) 229–234, doi:10.1016/S0022-2860(01)00638-X.
[11] S. Chena, Meng. Liub, Y. Yub, J. Wang, Room-temperature synthesis of fluorescent carbon-based nanoparticles and their application in multidimensional sensing, Sens. Actuat. B 288 (2019) 749–756, doi:10.1016/j.snb.2019.03.067.
[12] F. Cuenú, R. Abonia, A. Bolaños, A. Cabrera, Synthesis, structural elucidation and catalytic activity toward a model Mizoroki-Heck C-C coupling reaction of the pyrazolic Tröger's base $Pd_4Cl_8(PzTB)_2$ complex, J. Organomet. Chem. 696 (2011) 1834–1839, doi:10.1016/j.jorganchem.2011.02.016.
[13] S. Nieto, J. Pérez, L. Riera, V. Riera, D. Miguel, J.A. Golen, A.L. Rheingold, Pyrazole complexes as anion receptors: effects of changing the metal, the pyrazole substitution pattern, and the number of pyrazole ligands, Inorg. Chem. 46 (2007) 3407–3418, doi:10.1021/ic0700046.
[14] S. Babaee, M. Zarei, H. Sepehrmansourie, M.A. Zolfigol, S. Rostamnia, Synthesis of Metal−Organic Frameworks MIL-101(Cr)NH_2 Containing Phosphorous Acid Functional Groups: application for the Synthesis of *N*Amino-2-pyridone and Pyrano [2,3c]pyrazole Derivatives via a Cooperative Vinylogous Anomeric-Based Oxidation, ACS Omega 58 (2020) 6240–6249, doi:10.1021/acsomega.9b02133.
[15] W.A. Zoubi, Biological activities of Schiff bases and their complexes: a review of recent works, Int. J. Org. Chem. 03 (2013) 73–95.
[16] W.A. Zoubi1, A.A. Salih Al-Hamdani, S.D. Ahmed, Y.G. Ko, Synthesis, characterization, and biological activity of Schiff bases metal complexes, J. Phys. Org. Chem. 31 (2017) e3752, doi:10.1002/poc.3752.
[17] J.M. Mir, S.A. Majid, A.H. Shalla, Enhancement of Schiff base biological efficacy by metal coordination and introduction of metallic compounds as anticovid candidates: a simple overview, Rev. Inorg. Chem. 0 (2021) 1–13, doi:10.1515/revic-2020-0020.
[18] B.P. Mathew, M. Nath, Recent Approaches to Antifungal Therapy for Invasive Mycoses, Chem. Med. Chem. 4 (2009) 310–323, doi:10.1002/cmdc.200800353.
[19] F. Cuenú, A. Restrepo-Acevedo, M. Isabel-Murillo, J.E. Torres, R. Moreno-Fuquen, R. Abonia, A.R. Kennedy, J.C. Tenorio, C.W. Lehmann, Synthesis, structural characterization, and theoretical studies of new pyrazole (*E*)-2-{[(5-(*tert-butyl*)-1*H-pyrazol*-3-*yl*)*imino*]methyl}phenol and (*E*)-2-{[(1-(4-*bromophenyl*)-3-(*tert-butyl*)-1*H-pyrazol*-5-*yl*]imino]methyl}phenol, J. Mol. Struct. 1184 (2019) 59–71, doi:10.1016/j.molstruc.2019.02.004.
[20] F. Cuenú, J. Londoño Salazar, J.E. Torres, R. Abonia, R.F. D'Vries, Synthesis, structural characterization and theoretical studies of a new Schiff base 4-(((3-(*tert*-Butyl)-(1 phenyl)pyrazol-5-yl)imino)methyl)phenol, J. Mol. Struct. 1152 (2018) 163–176, doi:10.1016/j.molstruc.2017.09.078.
[21] R. Moreno Fuquen, F. Cuenú, J.E. Torres, G. De la Vega, E. Galarza, R. Abonia, A.R. Kennedy, Presence of $\pi\ldots\pi$ and C−H…π interactions in the new Schiff base 2-{(*E*)-[(3-*tert-butyl*-1-*phenyl*-1*H-pyrazol*-5-*yl*)*imino*]methyl}phenol: experimental and DFT computational studies, J. Mol. Struct. 1150 (2017) 366–373, doi:10.1016/j.molstruc.2017.08.093.
[22] F. Cuenú, N. Muñoz Patiño, J.E. Torres, R. Abonia, R.A. Toscano, J. Cobo, The new 3-(*tert*-butyl)-1-(2-nitrophenyl)-1*H*-pyrazol-5-amine: experimental and computational studies, J. Mol. Struct. 1148 (2017) 557–567, doi:10.1016/j.molstruc.2017.07.038.
[23] S. Hernández, F. Cuenú, R. Abonia, A. Cabrera, 3-(*tert*-butyl)-1-(3-nitrophenyl)-1*H*-pyrazol-5-amine, Acta Cryst. E68 (2012) 3171, doi:10.1107/S1600536812042791.
[24] K. Nepali, H. Lee, J. Liou, Nitro-group-containing drugs, J. Med. Chem. 62 (2019) 2851–2893, doi:10.1021/acs.jmedchem.8b00147.
[25] S. Ray, D.F. Kreitler, A.M. Gulick, A.S. Murkin, The Nitro Group as a Masked Electrophile in Covalent Enzyme Inhibition, ACS Chem. Biol. 13 (2018) 1470–1473, doi:10.1021/acschembio.8b00225.
[26] Q. Liu, Z. Liu, W. Hua, S. Gou, Discovery of 6–(7-Nitro-2,1,3-benzoxadiazol-4-ylthio)hexanol derivatives as glutathione transferase inhibitors with favorable selectivity and tolerated toxicity, J. Med. Chem. 64 (2021) 1701–1712, doi:10.1021/acs.jmedchem.0c02048.
[27] S. Patterson, S. Wyllie, Nitro drugs for the treatment of trypanosomatid diseases: past, present, and future prospects, Trends Parasitol. 30 (2014) 289–298, doi:10.1016/j.pt.2014.04.003.
[28] A. Jezuita, K. Ejsmont, H. Szatylowicz, Substituent effects of nitro group in cyclic compounds, Struct. Chem. 32 (2021) 179–203, doi:10.1007/s11224-020-01612-x.
[29] J.N. Low, J. Cobo, R. Abonia, J. Quiroga, C. Glidewell, 5-Amino-3-*tert*-butyl-1-(4-nitro-phenyl)-1*H*-pyrazole forms hydrogen bonded sheets of alternating (20) and (32) rings, Acta Cryst. C60 (2004) 194–195, doi:10.1107/s0108270104000678.
[30] C. Lee, W. Yang, R.G. Parr, Development of the Colle-Salvetti correlation-energy formula into a functional of the electron density, Phys. Rev. B 37 (1988) 785–789, doi:10.1103/physrevb.37.785.
[31] M.J. Frisch, G.W. Trucks, H.B. Schlegel, G.E. Scuseria, M.A. Robb, J.R. Cheeseman, G. Scalmani, V. Barone, B. Mennucci, G.A. Petersson, H. Nakatsuji, M. Caricato, X. Li, H.P. Hratchian, A.F. Izmaylov, J. Bloino, G. Zheng, J.L. Sonnenberg, M. Hada, M. Ehara, K. Toyota, R. Fukuda, J. Hasegawa, M. Ishida, T. Nakajima, Y. Honda, O. Kitao, H. Nakai, T. Vreven, J.A. Montgomery Jr., J.E. Peralta, F. Ogliaro, M. Bearpark, J.J. Heyd, E. Brothers, K.N. Kudin, V.N. Staroverov, R. Kobayashi, J. Normand, K. Raghavachari, A. Rendell, J.C. Burant, S.S. Iyengar, J. Tomasi, M. Cossi, N. Rega, J.M. Millam, M. Klene, J.E. Knox, J.B. Cross, V. Bakken, C. Adamo, J. Jaramillo, R. Gomperts, R.E. Stratmann, O. Yazyev, A.J. Austin, R. Cammi, C. Pomelli, J.W. Ochterski, R.L. Martin, K. Morokuma, V.G. Zakrzewski, G.A. Voth, P. Salvador, J.J. Dannenberg, S. Dapprich, A.D. Daniels, Ö. Farkas, J.B. Foresman, J.V. Ortiz, J. Cioslowski, D.J. Fox, Gaussian 09, Revision D.01, Gaussian, Inc., Wallingford CT, 2013.
[32] M.H. Jamróz, Vibrational Energy Distribution Analysis: VEDA 4, program, Warsaw, 2004–2010.
[33] N.M. O'Boyle, A.L. Tenderholt, K.M. Langner, cclib: a library for package-independent computational chemistry algorithms, J. Comput. Chem. 29 (2008) 839–845 http://dx.doi.org/10.1002/jcc.20823.
[34] AgilentCrysAlis PRO, Agilent Technologies Ltd, Yarnton, Oxfordshire, England, 2014.
[35] SAINT, version 6.28a; Bruker AXS Inc.,: Madison, Wisconsin, USA (2001).

[36] Bruker APEX2 Software Package Bruker AXS, Madison (2006)
[37] O.V. Dolomanov, L.J. Bourhis, R.J. Gildea, J.A.K. Howard, H. Puschmann, OLEX2: a complete structure solution, refinement and analysis program, J. Appl. Cryst. 42 (2009) 339–341, doi:10.1107/S0021889808042726.
[38] F. Macrae, P.R. Edgington, P. McCabe, E. Pidcock, G.P. Shields, R. Taylor, M. Towler, J.V. Streek, Mercury: visualization and analysis of crystal structures, J. Appl. Crystallogr. 41 (2008) 466–470, doi:10.1107/s002188980600731x.
[39] K. Brandenburg, H. Putz, DIAMOND- crystal and molecular structure visualization, Crystal Imp. 102 (2006) 53227 Bonn, Germany.
[40] CLSI, in: Clinical and Laboratory Standards Institute. Method M27-A3, 3rd ed, 28, Wayne, Ed.; NCCLS, Pennsylvania, 2008, pp. 1–25.
[41] O. Trott, A.J. Olson, AutoDock Vina: improving the speed and accuracy of docking with a new scoring function, efficient optimization and multithreading, J. Comput. Chem. 31 (2010) 455–461, doi:10.1002/jcc.21334.
[42] G.M. Morris, R. Huey, W. Lindstrom, M.F. Sanner, R.K. Belew, D.S. Goodsell, A.J. Olson, Autodock4 and AutoDockTools4: automated docking with selective receptor flexibility, J. Comput. Chem. 16 (2009) 2785–2791, doi:10.1002/jcc.21256.
[43] A. Ghadjari, R.C. Matthews, J.P. Burnie, Epitope mapping Candida albicans proteinase (SAP 2), FEMS Microbiol. Immunol. 19 (2006) 115–123, doi:10.1111/j.1574-695X.1997.tb01080.x.
[44] Dassault Systèmes BIOVIADiscovery Studio Visualizer, v16.1.0.15350, Dassault Systèmes, San Diego, 2015.
[45] M.D. Hanwell, D.E. Curtis, D.C. Lonie, T. Vandermeersch, E. Zurek, G.R. Hutchison, Avogadro: an advanced semantic chemical editor, visualization, and analysis platform, J. Cheminfor. (2012) 4–17, doi:10.1186/1758-2946.
[46] H. Ni, Y. Zhang, F. Zhang, J. Zhao, L. Wu, X. Chu, Synthesis, structural characterization and theoretical approach of 3-(2,6-dichlorobenzyl)-5-methyl-*N*-nitro-1,3,5-oxadiazinan-4 imine, Spectrochim. Acta. A 138 (2015) 648–659, doi:10.1016/j.saa.2014.11.058.
[47] F. Jensen, Introduction to Computational Chemistry, Wiley, New York, 1999.
[48] A.F. Cruz, A.S. López, A.G. Ríos, F. Cuenú, C.E. Rozo, Experimental and theoretical studies on the structure and spectroscopic properties of (*E*)-1-(2-aminophenyl)-3-(pyridine-4-yl) prop-2-en-1-one, J. Mol. Struct. 1098 (2015) 216–228, doi:10.1016/j.molstruc.2015.06.009.
[49] K. Bahgat, A.G. Ragheb, Analysis of vibrational spectra of 8-hydroxyquinoline and its 5,7-dichloro, 5,7-dibromo, 5,7-diiodo and 5,7-dinitro derivatives based on density functional theory calculations, Cent. Eur. J. Chem. 5 (2007) 201–220, doi:10.2478/s11532-006-0061-x.
[50] H. Saleem, S. Subashchandrabose, Y. Erdogdu, V. Thanikachalam, J. Jayabharathi, FT-IR, FT-Raman spectral and conformational studies on (*E*)-2-(2-hydroxybenzylidenamino)-3-(1*H*-indol-3yl) propionic acid, Spectrochim. Acta. A 101 (2013) 91–99, doi:10.1016/j.saa.2012.09.023.
[51] A. Makal, W. Schilf, B. Kamieński, A. Szady-Chelmieniecka, E. Grech, K. Woźniak, Hydrogen bonding in Schiff bases–NMR, structural and experimental charge density studies, Dalton Trans. 40 (2011) 421–430, doi:10.1039/C0DT00298D.
[52] G. Socrates, Infrared and Raman Characteristic Group Frequencies: Tables and Charts (Third ed.), John Wiley & Sons, Ltd, Chichester, UK, 2004.
[53] M.M. Iftime, S. Morariu, L. Marin, Salicyl-imine-chitosan hydrogels: supramolecular architecturing as a crosslinking method toward multifunctional hydrogels, Carbohydr. Polym. 165 (2017) 39–50, doi:10.1016/j.carbpol.2017.02.027.
[54] I. Fleming, Frontier Orbitals and Organic Chemical Reactions, John Wiley & Sons, New York, 1976, doi:10.1002/nadc.19770250113.
[55] M.J. Frisch, J.A. Pople, J.S. Binkley, Self-consistent molecular orbital methods 25. Supplementary functions for Gaussian basis sets, Chem. Phys. 80 (1984) 3265–3269, doi:10.1063/1.447079.
[56] N. Subramanian, N. Sundaraganesan, J. Jayabharathi, Molecular Structure, spectroscopic (FT-IT, FT-Raman, NMR UV) studies and first-order molecular hyperpolarizabilities of 1,2-bis(3-methoxy-4-hydroxybenzylidene)hydrazine by density functional method, Spectrochim. Acta. A 76 (2010) 259–269, doi:10.1016/j.saa.2010.03.033.
[57] K.M. Al-Ahmary, M.S. Al-Enezi, M.M. Habeeb, Molecular structure and spectroscopic properties of novel manganese (II) complex with sulfamethazine drug, J. Mol. Struct. 1035 (2013) 114–123, doi:10.1016/j.molstruc.2012.09.048.
[58] K.M. Al-Ahmary, M.M. Habeeb, A.H. AlObidan, Charge transfer complex between 2,3-diaminopyridine with chloranilic acid. Synthesis, characterization and DFT, TD-DFT computational studies, Spectrochim. Acta A. Mol. Biomol. Spectrosc. 196 (2018) 274-255, doi:10.1016/j.saa.2018.02.025.
[59] Z. Demircioğlu, G. Kaştaş, Ç.A. Kaştaş, R. Frank, X.R.D. Spectroscopic, Hirshfeld surface and DFT approach (chemical activity, ECT, NBO, FFA, NLO, MEP, NPA& MPA) of (*E*)-4-bromo-2-[(4-*bromophenylimino*)*methyl*]-6-ethoxyphenol, J. Mol. Struct. 1191 (2019) 129–137, doi:10.1016/j.molstruc.2019.03.060.
[60] G. Moghadam, F. Tirgir, A.H. Reshak, M. Khorshidi, Specific features of 3, 6-bis (4-hydroxy phenyl)-piperazine-2, 5-dione (BHPPD) diphenolic monomer and compered with toxic industrial bisphenol-A (BPA): DFT calculation, Mater. Chem. Phys. 236 (2019) 121780, doi:10.1016/j.matchemphys.2019.121780.
[61] R. Payal, M.K. Saroj, N. Sharma, R.C. Rastogi, Photophysical behavior of some thymol based Schiff bases using absorption and fluorescence spectroscopy, J. Luminesc. 198 (2018) 92–102, doi:10.1016/j.jlumin.2018.02.007.
[62] G. Garber, An overview of fungal infections, Drugs 61 (2001) 1–12, doi:10.2165/00003495-200161001-00001.
[63] T. Patterson, Advances and challenges in management of invasive mycoses, Lancet 366 (2005) 1013–1025, doi:10.1016/S0140-6736(05)67381-3.
[64] D. Kontogiannis, E. Mantadakis, G. Smonis, Systemic mycoses in the immunocompromised host: an update in antifungal therapy, J. Hosp. Infect. 53 (2003) 243–258, doi:10.1053/jhin.2002.1278.
[65] N. Singh, Treatment of opportunistic mycoses: how long is long enough? Lancet Infect. Dis. 3 (2003) 703–708, doi:10.1016/s1473-3099(03)00802-8.
[66] F. De Bernardis, A. Cassone, J. Sturtevant, R. Calderone, Expression of Candida albicans SAP1 and SAP2 in experimental vaginitis, Infect. Immun. 63 (1995) 1887–1892, doi:10.1128/iai.63.5.1887-1892.1995.
[67] P.T. Marcyk, E.V. Leblanc, D.A. Kuntz, A.O. Xue, F. Trilles, R. Bengtson, S. Kenney, T.M.G. Huang, D.S. Robbins, N. Williams, N.S. Krysan, D.J. Privé, G.G. Whitesell, L. Cowen, L.E. Brown, E. Lauren, Fungal-selective resorcylate aminopyrazole Hsp90 inhibitors: optimization of whole-cell anticryptococcal activity and insights into the structural origins of cryptococcal selectivity, J. Med. Chem. 64 (2021) 1139–1169, doi:10.1021/acs.jmedchem.0c01777.
[68] C.S. Leung, S.S.F. Leung, J. Tirado-Rives, W.L. Jorgensen, Methyl effects on protein-ligand binding, J. Med. Chem. 55 (2012) 4489–4500, doi:10.1021/jm3003697.